

Magnetization plateaus and enhanced magnetocaloric effect of a spin-1/2 Ising-Heisenberg and Heisenberg double sawtooth ladder with four-spin interaction


Hamid Arian Zad ^{1,2}, Vadim Ohanyan ^{3,4}, Azam Zoshki ² and Jozef Strečka ²

¹*A.I. Alikhanyan National Science Laboratory, 0036 Yerevan, Armenia*

²*Department of Theoretical Physics and Astrophysics, Faculty of Science, P. J. Šafárik University, Park Angelinum 9, 041 54 Košice, Slovak Republic*

³*Laboratory of Theoretical Physics, Yerevan State University, Alex Manoogian 1, 0025 Yerevan, Armenia*

⁴*CANDLE, Synchrotron Research Institute, 31 Acharyan Str., 0040 Yerevan, Armenia*

 (Received 8 July 2023; accepted 31 August 2023; published 19 October 2023; corrected 26 July 2024)

The ground state, entropy, and magnetic Grüneisen parameter of the antiferromagnetic spin-1/2 Ising-Heisenberg model on a double sawtooth ladder are rigorously investigated using the classical transfer-matrix technique. The model includes the XXZ interaction between the interstitial Heisenberg dimers, the Ising coupling between nearest-neighbor spins of the legs and rungs, and additional cyclic four-spin Ising term in each square plaquette. For a particular value of the cyclic four-spin exchange, we found in the ground-state phase diagram of the Ising-Heisenberg ladder a quadruple point, at which four different ground states coexist together. During an adiabatic demagnetization process, a fast cooling accompanied with an enhanced magnetocaloric effect can be detected near this quadruple point. The ground-state phase diagram of the Ising-Heisenberg ladder is confronted with the zero-temperature magnetization process of the purely quantum Heisenberg ladder, which is calculated by using exact diagonalization based on the Lanczos algorithm for a finite-size ladder of 24 spins and the density-matrix renormalization group simulations for a finite-size ladder with up to 96 spins. Some indications of the existence of intermediate magnetization plateaus in the magnetization process of the full Heisenberg model for a small but nonzero four-spin Ising coupling were found. The DMRG results reveal that the quantum Heisenberg double sawtooth ladder exhibits some quantum Luttinger spin-liquid phase regions that are absent in the Ising-Heisenberg counterpart model. Except this difference, the magnetic behavior of the full Heisenberg model is quite analogous to its simplified Ising-Heisenberg counterpart and, hence, may bring insight into the fully quantum Heisenberg model from rigorous results for the Ising-Heisenberg model.

DOI: [10.1103/PhysRevE.108.044132](https://doi.org/10.1103/PhysRevE.108.044132)

I. INTRODUCTION

The variation of external magnetic fields causing an adiabatic change in the temperature of magnetic materials is referred to as the magnetocaloric effect (MCE). This phenomenon, particularly adiabatic demagnetization, constitutes a fundamental element in magnetic refrigeration technology. The amplified MCE holds significant promise for both room-temperature and low-temperature refrigeration applications, as extensively discussed in recent reviews, i.e., see Refs. [1,2]. Moreover, the MCE plays an important role in unraveling the intricate phase diagrams of magnetic materials within the magnetic field–temperature plane. This is achieved by harnessing the magnetocaloric anomalies that emerge during magnetic phase transitions. This approach not only provides deep insights into the behavior of magnetic materials but also enhances our understanding of their complex properties and characteristics. The standard quantity to characterize the MCE is the so-called magnetic Grüneisen parameter Γ related to the adiabatic cooling rate through the formula

$$\Gamma = \frac{1}{T} \left(\frac{\partial T}{\partial B} \right)_S = -\frac{T}{C_B} \left(\frac{\partial S}{\partial B} \right)_T = -\frac{T}{C_B} \left(\frac{\partial M}{\partial T} \right)_B, \quad (1)$$

where C_B is the heat capacity at the constant magnetic field B , T is the temperature, and M is the magnetization.

In recent decades, a lot of theoretical investigations have brought insight into the MCE within the realm of low-dimensional quantum and Ising spin models [3–19]. These endeavors have yielded exact outcomes within these models, uncovering crucial aspects of the MCE. Furthermore, alongside the exploration of adiabatic cooling rates, significant insights into the MCE have emerged from the analysis of isentropes within the temperature-magnetic field plane. Such plots provide vital information about the intricate behavior and characteristics of the magnetocaloric phenomenon.

A large number of exact results have already been made in understanding the MCE within the various Ising-Heisenberg spin models [14–19]. These models share common characteristics: a systematic alternation between small clusters of quantum Heisenberg spins and Ising spins. This arrangement ensures that the local Hamiltonians for individual blocks exhibit commutativity, enabling an exact solution of the Ising-Heisenberg spin model through the utilization of the generalized classical transfer-matrix method.

Although the periodic alternation of Heisenberg and Ising spins is infrequent in real magnetic materials, a few notable examples of exactly solvable Ising-Heisenberg spin chains have provided remarkably accurate insights into the magnetic properties of specific compounds. Noteworthy instances include $\text{Cu}(\text{3-Clpy})_2(\text{N}_3)_2$ [20], $[(\text{CuL})_2\text{Dy}][\text{Mo}(\text{CN})_8]$ [21,22],

[Fe(H₂O)(L)][Nb(CN)₈][Fe(L)] [23], Dy(NO₃)(DMSO)₂Cu(opba)(DMSO)₂ [24,25], [CuMn(L)][Fe(bpb)(CN)₂] ClO₄ H₂O [26], and [Dy(hfac)₂(CH₃OH)]₂[Cu(dmg)(Hdmg)]₂ [27,28].

Several observations arise in connection with the four-spin Ising coupling, which can alternatively be viewed as the Ising limit arising from the cyclic permutation of quantum spins or as a higher-order exchange process. Indeed, these exchange terms have been conclusively shown to have paramount significance in comprehending the magnetic properties of solid ³He [29], as well as certain cuprate materials (see Ref. [30] and the cited references therein).

The Ising and mixed Ising-Heisenberg spin models featuring the four-spin Ising coupling (product of four Ising variables) have gathered attention in several studies. They have been explored both as the Ising limit emerging from the four-spin cyclic permutation and in independent frameworks [8,31–39]. Moreover, investigations of the Ising-Heisenberg model on structures such as the sawtooth chain [40–42], the two-leg ladder [43,44], and the tetrahedral chain [15] have been conducted in earlier works.

Exact solutions have been achieved for both the spin-1/2 and mixed spin-(1/2,1) Ising-Heisenberg double sawtooth ladders possessing cyclic four-spin interactions. These solutions have been attained through a modified classical transfer-matrix technique, yielding valuable insights into their ground-state phase diagrams, as well as their magnetic and thermodynamic properties. These findings have been documented in previous studies [37–39].

Moreover, a comprehensive investigation into the ground-state phase diagram has been undertaken for the spin-1/2 Heisenberg model on a two-leg ladder. This analysis, conducted in the absence of an external field, was presented in Ref. [45]. Of particular note is the discovery of a diverse ground-state phases, encompassing rung-singlet, saturated ferromagnetic states and an intriguing Luttinger spin-liquid phase. Interesting phenomena observed within ladder-type models have initiated a surge of research activity aimed towards unraveling the magnetic excitations and ground-state phase diagram of frustrated spin ladders accounting for the next-nearest-neighbor interactions [46].

The intriguing frustrated double sawtooth ladder, as depicted in Fig. 1, presents an appealing spin model due to its potential to give rise to a thought-provoking paradox resembling a two-leg ladder with next-nearest-neighbor interactions along the legs. This unique attribute arises from the geometric arrangement of the model, intertwining two frustrated sawtooth spin chains by means of distinct rungs [47–49].

While previous investigations have unveiled a lot of captivating magnetic characteristics within analogous quantum spin ladder models, certain pivotal insights still remain controversial. Notably, aspects like the zero-temperature magnetization, MCE, and the intricacies of the cooling/heating process within the double sawtooth ladder, with nonzero four-spin Ising interaction, persist as unresolved issues to deal with. Consequently, the present study focuses on the MCE of the Ising-Heisenberg double sawtooth ladder, with a particular emphasis on the critical cyclic four-spin Ising interaction point where four distinct ground states coexist.

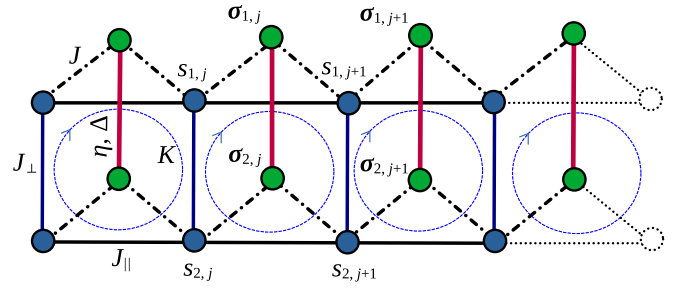


FIG. 1. A schematic illustration of the magnetic structure of the frustrated spin-1/2 double sawtooth ladder. The balls denote spin-1/2 particles. Green balls represent Heisenberg spins that are connected with each other with red solid lines. The dark-blue balls show Ising spins. The blue dashed circle in each square plaquette denotes four-spin Ising coupling.

Furthermore, an in-depth examination of the magnetization process of the complete Heisenberg double sawtooth ladder is conducted using the full exact diagonalization (ED) method. To achieve this, we adapted the computational capabilities of the QUSPIN package [50,51] for solving finite-size ladders comprising of 24 spins. Additionally, we employ the ITENSOR package [52] to implement the density matrix renormalization group (DMRG) method, which relies on tensor network algorithms to diagonalize larger ladders composed of 64, 80, and 96 spins while conserving the total quantum number S_T^z . Of particular interest is the detailed verification of how the magnetization behavior of the full Heisenberg double sawtooth ladder is influenced by the Heisenberg exchange anisotropy and the four-spin Ising coupling. This exploration seeks to shed light on the intricate interplay of these factors within the ladder's magnetic properties.

The paper is structured as follows. In the upcoming section, we provide a comprehensive explanation of the spin-1/2 Ising-Heisenberg model on the double sawtooth ladder. We outline the analytical approach employed to tackle this model. Subsequently, we provide a complete analysis of the ground-state phase diagram and critical phenomena inherent in the Ising-Heisenberg model. This section explores the interplay of entropy and the Grüneisen parameter concerning magnetic field and temperature for various fixed parameter configurations. The influence of the four-spin Ising coupling on the adiabatic demagnetization process within the Ising-Heisenberg model is also investigated. Moving on to Sec. III, we introduce a full quantum Heisenberg model on the frustrated double sawtooth ladder. We then proceed to elaborate on the numerical techniques we employ, namely, the ED method based on the Lanczos algorithm and the DMRG method. These approaches are adapted for investigating the zero-temperature magnetization process of the full Heisenberg double sawtooth ladder. Lastly, in Sec. IV, we summarize our findings and insights.

II. ISING-HEISENBERG DOUBLE SAWTOOTH LADDER

Let us consider a frustrated spin-1/2 Ising-Heisenberg double sawtooth ladder (or decorated two-leg ladder) with four-spin Ising coupling as schematically illustrated in Fig. 1. The total Hamiltonian of this model is given by the following

expression:

$$\begin{aligned}
H = & \sum_{j=1}^N [(\boldsymbol{\sigma}_{1,j} \cdot \boldsymbol{\sigma}_{2,j})_{\eta,\Delta} \\
& + \sum_{a=1,2} (J_{\parallel} s_{a,j} s_{a,j+1} + J \sigma_{a,j}^z (s_{a,j} + s_{a,j+1})) \\
& + J_{\perp} s_{1,j} s_{2,j} + K s_{1,j} s_{1,j+1} s_{2,j} s_{2,j+1} \\
& - B \sum_{a=1,2} (\sigma_{a,j}^z + s_{a,j})], \quad (2)
\end{aligned}$$

where N denotes the total number of unit cells, $s_{a,j}$ are Ising spin variables taking values 1 or -1 , B is the external magnetic field applied along the z direction, and each pair of quantum spins $\boldsymbol{\sigma}_{1,j}$ and $\boldsymbol{\sigma}_{2,j}$ interacts via the XXZ exchange coupling defined through the Pauli matrices σ_i^{α} ($\alpha = x, y, z$) as follows:

$$(\boldsymbol{\sigma}_{1,j} \cdot \boldsymbol{\sigma}_{2,j})_{\eta,\Delta} = \eta(\sigma_{1,j}^x \sigma_{2,j}^x + \sigma_{1,j}^y \sigma_{2,j}^y) + \Delta \sigma_{1,j}^z \sigma_{2,j}^z. \quad (3)$$

The coupling constants J_{\perp} and J_{\parallel} are the Ising-type couplings on the rungs and along the legs, respectively, and the coupling constant K accounts for the four-spin Ising term in each square plaquette composed of four Ising spins belonging to two neighboring unit blocks. The complete elaboration of this term can be found in Appendix A. The coupling constant J is the Ising coupling between the Ising spins on the legs and two quantum spins of the interstitial Heisenberg dimer on the tips. This coupling is supposed to include only the z component of the quantum spins. Let us mention that all parameters here are supposed to be dimensionless, taking $J_{\parallel} = J_{\perp}$ as energy unit.

A. The exact solution in terms of the generalized classical transfer-matrix method

Let us present a few crucial steps of the analytical procedure used to calculate the partition function Z of the model within the generalized classical transfer-matrix technique:

$$\begin{aligned}
Z = & \sum_{(s_1)} \sum_{(s_2)} \text{Tr}_{(\boldsymbol{\sigma}_1, \boldsymbol{\sigma}_2)} e^{-\beta H} \\
= & \sum_{(s_1)} \sum_{(s_2)} \prod_{j=1}^N \mathbf{T}(s_{1,j}, s_{2,j} | s_{1,j+1}, s_{2,j+1}) = \text{Tr} \mathbf{T}^N, \quad (4)
\end{aligned}$$

where the 4×4 transfer matrix is given by

$$\begin{aligned}
\mathbf{T}(s_{1,j}, s_{2,j} | s_{1,j+1}, s_{2,j+1}) \\
= & \exp\{-\beta H^1(s_{1,j}, s_{2,j} | s_{1,j+1}, s_{2,j+1})\} \\
& \times W(s_{1,j}, s_{2,j} | s_{1,j+1}, s_{2,j+1}), \quad (5)
\end{aligned}$$

where the Ising part of the system's Hamiltonian reads

$$\begin{aligned}
H^1(s_{1,j}, s_{2,j} | s_{1,j+1}, s_{2,j+1}) \\
= & J_{\parallel} \sum_{a=1,2} s_{a,j} s_{a,j+1} + J_{\perp} s_{1,j} s_{2,j} \\
& + K s_{1,j} s_{1,j+1} s_{2,j} s_{2,j+1} - B \sum_{a=1,2} s_{a,j}, \quad (6)
\end{aligned}$$

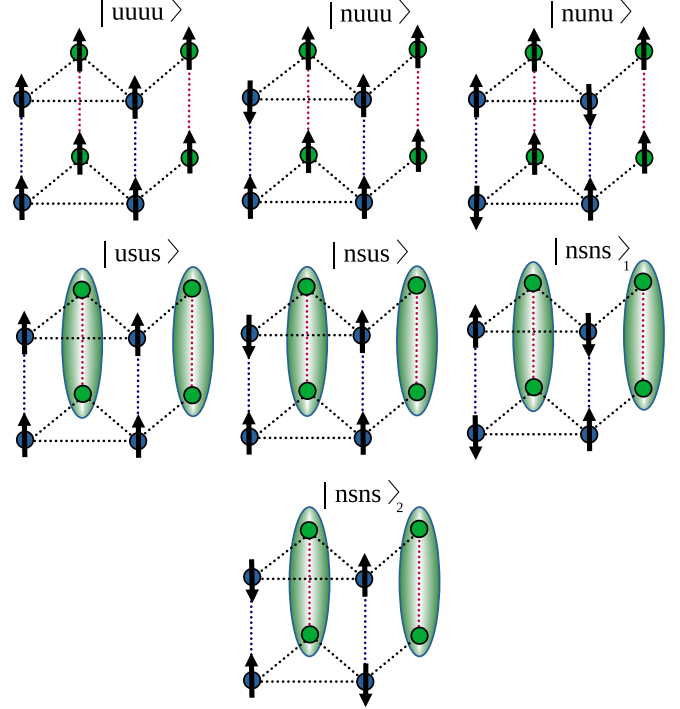


FIG. 2. The spin configurations of the spin-1/2 double sawtooth ladder associated to the possible ground states Eq. (8). Each panel indicates spin arrangement of two successive unit blocks that are repeated throughout the ladder. Tick arrows represent the spin orientations, whereas oval shapes stand for the Heisenberg dimers in quasisinglet state $|\varphi_2\rangle$. Notations in the kets denote the orientation of the two spins on each rung such that up means both spins of the same rung are up, while n indicates that one spin of the rung is up and another one is down, and s means that the state of the two spins on the identical rung is quasi-singlet state $|\varphi_2\rangle$.

and the Boltzmann factor of the quantum dimer, W , is

$$W(s_{1,j}, s_{2,j} | s_{1,j+1}, s_{2,j+1}) = \sum_{l=1}^4 e^{-\beta \varepsilon_n(s_{1,j}, s_{2,j} | s_{1,j+1}, s_{2,j+1})},$$

in which $\varepsilon_n(s_{1,j}, s_{2,j} | s_{1,j+1}, s_{2,j+1})$ with $n = 1, \dots, 4$ are the eigenvalues of the quantum part of the Hamiltonian:

$$H^q = (\boldsymbol{\sigma}_{1,j} \cdot \boldsymbol{\sigma}_{2,j})_{\eta,\Delta} - \sum_{a=1,2} [B - J(s_{a,j} + s_{a,j+1})] \sigma_{a,j}^z. \quad (7)$$

The eigenvalues and eigenvectors of the quantum part of the total Hamiltonian Eq. (2) are given in Appendix B. They explicitly depend on the values of four Ising spin variables, interacting with the quantum spin dimer. They can be easily found by the straightforward diagonalization of the quantum Hamiltonian Eq. (7) in the standard Ising basis $\{|\uparrow\uparrow\rangle, |\uparrow\downarrow\rangle, |\downarrow\uparrow\rangle, |\downarrow\downarrow\rangle\}$.

B. Ground states

The system under consideration possesses several ground states, depending on its microscopic parameters, η , Δ , J_{\perp} , J , J_{\parallel} , K , and B . As the main goal of this section is to clarify the role of the Heisenberg exchange anisotropy Δ and four-spin Ising interaction K in the enhancement of the MCE of the

Ising-Heisenberg double sawtooth ladder, we here focus on a peculiar range of parameters, which admit special points in the ground-state phase diagram with a high degeneracy. The MCE is stronger around triple points and particularly around points of confluence of more phases [7]. We are going to examine the ground-state phase diagram, MCE, and cooling rate of the spin-1/2 Ising-Heisenberg double sawtooth ladder with nonzero four-spin Ising interaction K . To provide a clear definition of the relevant ground states of the model, we demonstrate their special spin configurations in Fig. 2. Among these ground states, $|\text{usus}\rangle$, $|\text{nsus}\rangle$, $|\text{nsns}\rangle_1$, and $|\text{nsns}\rangle_2$ include the dimeric quasi-singlet state $|\varphi_2\rangle$ and are subject to the doubling of the unit cell, which is the manifestation of the quantum antiferromagnetic coupling along the alternating rungs. From this point of view, we compose the spin orientation of two successive unit cells in our notation. The relevant ground states with the corresponding magnetization values per unit cell are given by the following expressions:

$$\begin{aligned}
 |\text{uuuu}\rangle &= \prod_{i=1}^{N/2} |\uparrow\uparrow\rangle_{2i-1} \otimes |\varphi_4\rangle_{2i-1} \otimes |\uparrow\uparrow\rangle_{2i} \otimes |\varphi_4\rangle_{2i}, \\
 E_{\text{uuuu}} &= -4B + \Delta + 2J_{\parallel} + J_{\perp} + 4J + K, \quad M/M_s = 1, \\
 |\text{nuuu}\rangle &= \prod_{i=1}^{N/2} |\downarrow\uparrow\rangle_{2i-1} \otimes |\varphi_4\rangle_{2i-1} \otimes |\uparrow\uparrow\rangle_{2i} \otimes |\varphi_4\rangle_{2i}, \\
 E_{\text{nuuu}} &= -3B + \Delta + 2J - K, \quad M/M_s = \frac{3}{4}, \\
 |\text{nunu}\rangle &= \prod_{i=1}^{N/2} |\uparrow\downarrow\rangle_{2i-1} \otimes |\varphi_4\rangle_{2i-1} \otimes |\downarrow\uparrow\rangle_{2i} \otimes |\varphi_4\rangle_{2i}, \\
 E_{\text{nunu}} &= -2B + \Delta - 2J_{\parallel} - J_{\perp} + K, \quad M/M_s = \frac{1}{2}, \\
 |\text{usus}\rangle &= \prod_{i=1}^{N/2} |\uparrow\uparrow\rangle_{2i-1} \otimes |\varphi_2\rangle_{2i-1} \otimes |\uparrow\uparrow\rangle_{2i} \otimes |\varphi_2\rangle_{2i}, \\
 E_{\text{usus}} &= -2B - 2\eta - \Delta + 2J_{\parallel} + J_{\perp} + K, \quad M/M_s = \frac{1}{2}, \\
 |\text{nsus}\rangle &= \prod_{i=1}^{N/2} |\downarrow\uparrow\rangle_{2i-1} \otimes |\varphi_2\rangle_{2i-1} \otimes |\uparrow\uparrow\rangle_{2i} \otimes |\varphi_2\rangle_{2i}, \\
 E_{\text{nsus}} &= -B - \Delta - K - 2\sqrt{\eta^2 + J^2}, \quad M/M_s = \frac{1}{4}, \\
 |\text{nsns}\rangle_1 &= \prod_{i=1}^{N/2} |\uparrow\downarrow\rangle_{2i-1} \otimes |\varphi_2\rangle_{2i-1} \otimes |\downarrow\uparrow\rangle_{2i} \otimes |\varphi_2\rangle_{2i}, \\
 E_{\text{nsns}}^{(1)} &= -2\eta - \Delta - 2J_{\parallel} - J_{\perp} + K, \quad M/M_s = 0, \\
 |\text{nsns}\rangle_2 &= \prod_{i=1}^{N/2} |\downarrow\uparrow\rangle_{2i-1} \otimes |\varphi_2\rangle_{2i-1} \otimes |\uparrow\downarrow\rangle_{2i} \otimes |\varphi_2\rangle_{2i}, \\
 E_{\text{nsns}}^{(2)} &= -\Delta + 2J_{\parallel} - J_{\perp} - 2\sqrt{\eta^2 + 4J^2} + K, \quad M/M_s = 0.
 \end{aligned} \tag{8}$$

Here the following principles in the notation of ground states are adopted. The unit cell in the configurations with period

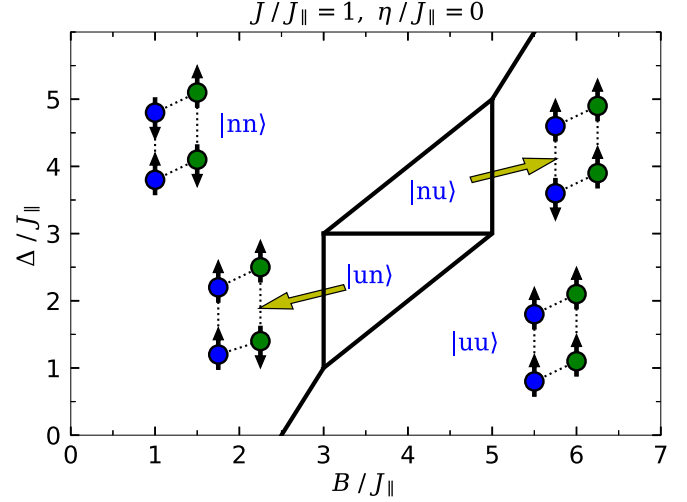


FIG. 3. Ground-state phase diagram of the pure Ising double sawtooth ladder in the $\Delta/J_{\parallel} - B/J_{\parallel}$ plane for $\eta/J_{\parallel} = 0$ and $J/J_{\parallel} = 1$.

doubling contains four pairs of spins; each pair is coupled together by a rung. Thus, for the two spins on a rung pointing up we use u, for the pair of spins pointing in opposite directions we use n, and finally for the quantum quasi-singlet state $|\varphi_2\rangle$ we use s.

For the case $\eta/J_{\parallel} = 0$, where $J_{\parallel} = J_{\perp}$ is assumed as an energy unit, the system is reduced to the simple Ising model with four different ground states $\{|\text{nn}\rangle, |\text{un}\rangle, |\text{nu}\rangle, |\text{uu}\rangle\}$ with boundaries shown by solid lines in Fig. 3. It can be realized from Eq. (8) that one obtains $A_{\pm} = 0$ for $\eta/J_{\parallel} = 0$ and $|\varphi_2\rangle \rightarrow |\uparrow\downarrow\rangle$, which implies that two ground states $\{|\text{nsns}\rangle_1, |\text{usus}\rangle\}$ collapse into simplified counterpart states $\{|\text{nn}\rangle, |\text{un}\rangle\}$. For better clarity, we also draw in Fig. 3 the spin orientation of a unit block of the Ising model corresponding to each ground state. It is quite clear that here the ground-state phase diagram of the pure Ising double sawtooth ladder is independent of the four-spin exchange coupling K/J_{\parallel} .

For the Ising-Heisenberg double sawtooth ladder ($\eta/J_{\parallel} \neq 0$), by simultaneous eigenenergy comparison of the four different ground states $|\text{nsus}\rangle$, $|\text{usus}\rangle$, $|\text{nunu}\rangle$, and $|\text{nuuu}\rangle$, one finds a straightforward expression for the exchange anisotropy Δ/J_{\parallel} , four-spin Ising interaction K/J_{\parallel} and B/J_{\parallel} such that these ground states coexist together at a quadruple point. The two ground states $|\text{nunu}\rangle$ and $|\text{usus}\rangle$ are degenerate whenever the following condition is satisfied:

$$\Delta_Q/J_{\parallel} = 2 + J_{\perp}/J_{\parallel} - \eta/J_{\parallel}. \tag{9}$$

In our calculations, we set $J_{\perp}/J_{\parallel} = \eta/J_{\parallel} = 1.0$, leading to $\Delta_Q/J_{\parallel} = 2.0$. We elucidate in Fig. 4(a) the two-body exchange coupling dependence of the special value of the four-spin Ising interaction at the quadruple point coordinates, i.e.,

$$K_Q/J_{\parallel} = \frac{1}{2}(\eta/J_{\parallel} + J/J_{\parallel} - \sqrt{(\eta/J_{\parallel})^2 + (J/J_{\parallel})^2}), \tag{10}$$

which depends only on η/J_{\parallel} and J/J_{\parallel} . Obviously, the maximum value of $K_Q^{\text{max}}/J_{\parallel} = \frac{1}{2}(2 - \sqrt{2}|\eta/J_{\parallel}|)$ occurs in the antiferromagnetic regime when $\eta/J_{\parallel} = J/J_{\parallel}$ (solid point on the top of curve). It is noteworthy that here we restrict

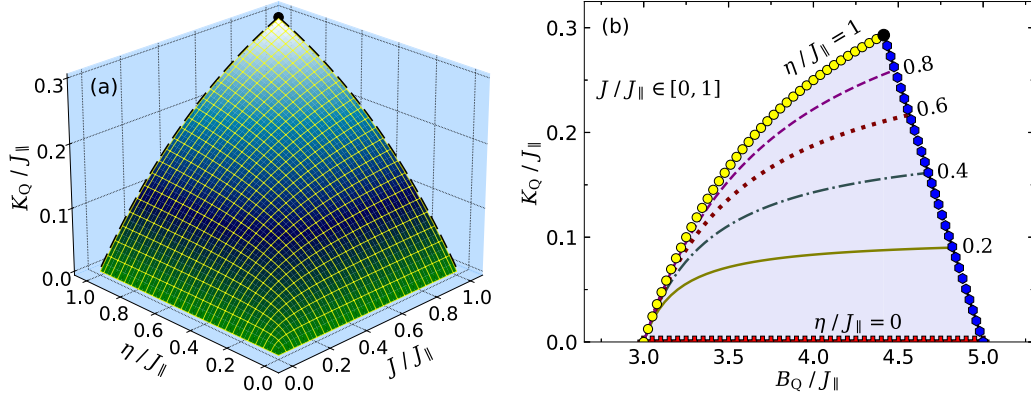


FIG. 4. (a) Topological representation of the critical four-spin exchange interaction Eq. (10) at which four ground states $|nsus\rangle$, $|usus\rangle$, $|nunu\rangle$, and $|nuuu\rangle$ coexist together at a quadruple point with magnetic field position $B_Q/J_{\parallel} = 3 + 2J/J_{\parallel} - 2K_Q/J_{\parallel}$. (b) The K_Q/J_{\parallel} as a function of the magnetic field position of the quadruple point B_Q/J_{\parallel} for $\eta/J_{\parallel}, J/J_{\parallel} \in [0, 1]$. The line marked with blue hexagons shows maximum amount of B_Q^{\max} and K_Q^{\max} for $J/J_{\parallel} = 1$ where η/J_{\parallel} varies from 0 (red crosses) up to 1 (yellow circles). K_Q as a function of B_Q is shown for a few selected values of η/J_{\parallel} by lines with different styles. Filled circle on top of curve plotted in(a) shows the coordination of the point $K_Q^{\max}/J_{\parallel} = \frac{1}{2}(2 - \sqrt{2}|\eta/J_{\parallel}|) \approx 0.2929$, assuming $\eta/J_{\parallel} = J/J_{\parallel} = +1$. This point is geometrically the same one on the ending point of the yellow curve plotted in (b) with $B_Q/J_{\parallel} = 4.4142$.

ourselves to the parameter region $0 \leq \{\eta/J_{\parallel}, J/J_{\parallel}\} \leq 1$ for simplicity. Furthermore, the magnetic field position of the quadruple point depends on the coupling constants J/J_{\parallel} and K_Q/J_{\parallel} as follows:

$$B_Q/J_{\parallel} = 3 + 2J/J_{\parallel} - 2K_Q/J_{\parallel}. \quad (11)$$

Figure 4(b) displays four-spin Ising interaction of the quadruple point K_Q/J_{\parallel} as a function of its magnetic field position B_Q/J_{\parallel} [see Eq. (11)] when J/J_{\parallel} is varied from 0 up to 1. It is noteworthy that the term K_Q/J_{\parallel} itself depends on the J/J_{\parallel} according to Eq. (10). It is quite clear from this figure that by increasing the interaction ratio J/J_{\parallel} , the quantity K_Q/J_{\parallel} increases and, accordingly, B_Q/J_{\parallel} increases. Lines with different styles demonstrate quantity K_Q/J_{\parallel} with respect to B_Q/J_{\parallel} for a few selected values of η/J_{\parallel} . All lines arise from the same minimum magnetic field point $B_Q^{\min}/J_{\parallel} = 3.0$ and terminate at different maximum magnetic field points. Regarding this, Eqs. (10) and (11) hold for each point of the shaded area of Fig. 4(b) where the coordinates of the quadruple point do not exceed this area. The line marked with blue hexagons manifests a descending behavior of B_Q^{\max}/J_{\parallel} with respect to the interaction ratio η/J_{\parallel} . In other words, when the exchange interaction ratio η/J_{\parallel} increases, the term B_Q^{\max}/J_{\parallel} moves towards lower values, while K_Q^{\max}/J_{\parallel} increases.

Keeping this fact in mind, we plot in Fig. 5 the ground-state phase diagram of the Ising-Heisenberg ladder for $\eta/J_{\parallel} = J/J_{\parallel} = 1.0$ and $K = K_Q$. To have a direct conjunction between Fig. 4(b) and Fig. 5, we have marked a particular point with a black circle on the upper bound of the yellow curve at $(K_Q^{\max}/J_{\parallel}, B_Q^{\max}/J_{\parallel}) \approx (0.2929, 4.4142)$, which indicates the position of the quadruple point appearing Fig. 5. For higher interaction ratio J/J_{\parallel} , four aforementioned ground states coexist together at higher magnetic field and higher four-spin Ising interaction [see a black circle on the yellow curve in Fig. 4(b)]. Moreover, there are two triple points at $(\Delta/J_{\parallel}, B/J_{\parallel}) \approx (0.595, 1.5858)$ and at $(\Delta/J_{\parallel}, B/J_{\parallel}) \approx (2.595, 5.5858)$, where three different ground states coexist together.

As a result, the position of the quadruple point moves towards higher magnetic field with increasing J/J_{\parallel} , while the position of the first triple point moves towards a lower magnetic field. Therefore, increasing J/J_{\parallel} leads to diminishing the boundary of phase $|nsns\rangle_1$ with zero magnetization and to increasing the boundary of phase $|nsus\rangle$ with $M/M_s = 1/4$. Other phase boundaries will remarkably change as well. In the next section, we investigate the MCE of the Ising-Heisenberg ladder near the first triple point at which the coexistence of three ground states $|nsns\rangle_1$, $|nsus\rangle$, and $|nunu\rangle$ occurs, then we compare the results with ones obtained for the MCE of the Ising-Heisenberg model close to the quadruple point.

In Fig. 6, we display the ground-state phase diagram of the Ising-Heisenberg double sawtooth ladder in the $K/J_{\parallel} - B/J_{\parallel}$ plane for the specific case $\Delta/J_{\parallel} = 2$ [see Eq. (9)], assuming $J/J_{\parallel} = \eta/J_{\parallel} = 1.0$. Under these

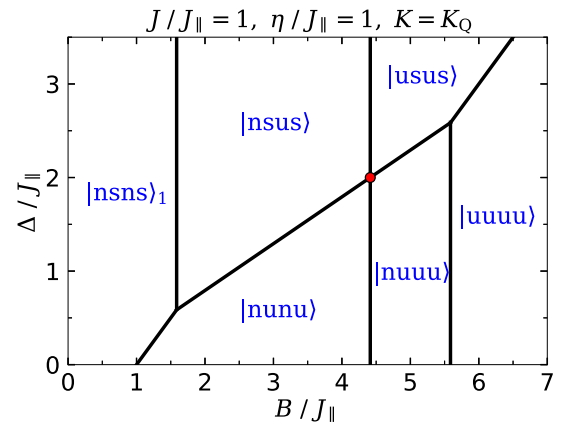


FIG. 5. Ground-state phase diagram of the Ising-Heisenberg double sawtooth ladder in the $\Delta/J_{\parallel} - B/J_{\parallel}$ plane for $\eta/J_{\parallel} = J/J_{\parallel} = 1$ and $K = K_Q \approx 0.2929$, where the quadruple point occurs at $(\Delta_Q/J_{\parallel} = 2.0, B_Q/J_{\parallel} \approx 4.4142)$. Red circle manifests the quadruple point.

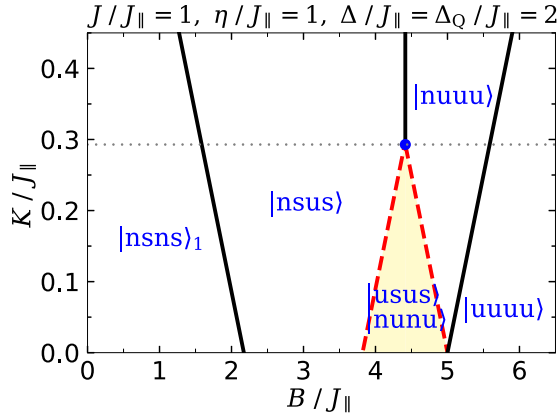


FIG. 6. Ground-state phase diagram of the spin-1/2 Ising-Heisenberg double sawtooth ladder in the $K/J_{\parallel} - B/J_{\parallel}$ plane for exchange interaction ratios $\eta/J_{\parallel} = J/J_{\parallel} = 1$, $\Delta/J_{\parallel} = 2$. Red broken lines represent the same phase boundary for the ground states $|nunu\rangle$ and $|usus\rangle$, which become degenerate when Eq. (9) holds for the interaction ratios J_{\perp}/J_{\parallel} and η/J_{\parallel} . Solid dot indicates the position of the quadruple point according to Eqs. (9)-(11) whose coordinates are $(K_Q/J_{\parallel}, B_Q/J_{\parallel}) \approx (0.2929, 4.4142)$. The horizontal dotted lines indicate the value K_Q/J_{\parallel} given by Eq. (10). We note that according to Eqs. (10) and (11) that hold for each point of the shaded area of Fig. 4(b), having $(K, B) = (K_Q, B_Q)$, thus the quadruple point is generated, if and only if, $\Delta/J_{\parallel} = \Delta_Q/J_{\parallel} = 2.0$.

circumstances, the aforementioned quadruple point appears in the ground-state phase diagram of the model such that the two ground states $|nunu\rangle$ and $|usus\rangle$ become degenerate, while Eq. (9) holds for the interaction ratios J_{\perp}/J_{\parallel} and η/J_{\parallel} . A shaded region delimited by red dashed lines identifies the coexistence region of these two degenerate ground states with the identical magnetization ($M/M_s = 1/2$). The solid point in Fig. 6 indicates the coordinates of the quadruple point.

It is demonstrated in Fig. 4(b) that the field coordinate of the quadruple point shifts towards lower magnetic field and lower four-spin Ising interaction values as the interaction ratio J/J_{\parallel} decreases. For example, the coordinates of the quadruple point in Fig. 6 are $(K_Q^{\max}/J_{\parallel}, B_Q^{\max}/J_{\parallel}) \approx (0.2929, 4.4142)$. Now, suppose $J/J_{\parallel} = 0.5$, the coordinates of the quadru-

ple point are $(K_Q/J_{\parallel}, B_Q/J_{\parallel}) \approx (0.19098, 3.62)$. One can see in Fig. 6(b) that there are three different first-order phase transitions in the ground-state phase diagram of the Ising-Heisenberg ladder for $K/J_{\parallel} = 0$ and $\Delta/J_{\parallel} = 2.0$. Apparently, state $|nsus\rangle$ with magnetization value $M/M_s = 1/4$ is the ground state of the system for moderate magnetic fields. Under this condition, state $|nuuu\rangle$ with magnetization value $M/M_s = 3/4$ still could not be the ground state of the Ising-Heisenberg double sawtooth ladder.

The ground-state phase diagram of the spin-1/2 Ising-Heisenberg model on the double sawtooth ladder in the $J/J_{\parallel} - B/J_{\parallel}$ plane is displayed in Fig. 7 for the parameter set $\eta/J_{\parallel} = \Delta/J_{\parallel} = 1$, supposing the isotropic interaction between the Heisenberg spins. By inspecting Fig. 6(a), one can find out that for the small but nonzero value of the four-spin Ising interaction ratio $0 < K/J_{\parallel} < 1$, the Ising-Heisenberg system shows a rich ground-state phase diagram. The phase boundary of ground state $|nuuu\rangle$ gradually broadens with increasing of the ratio K/J_{\parallel} , while the phase boundary of ground state $|nunu\rangle$ diminishes until it ultimately disappears [see Fig. 6(b)]. In addition, the four-spin exchange interaction gives rise to ground state $|nsus\rangle$, emergent in a ferromagnetic regime of the interaction ratio $J/J_{\parallel} < 0$. It could be concluded that the stability region of ground states $|nsus\rangle$ and $|nunu\rangle$ increases for $\eta/J_{\parallel} = \Delta/J_{\parallel} = 1$ with increasing of K/J_{\parallel} , while the region of ground state $|nunu\rangle$ decreases until it completely disappears.

C. Adiabatic (de)magnetization process of the spin-1/2 Ising-Heisenberg ladder

Recently, many authors have widely reported that various frustrated quantum spin systems exhibit an enhanced MCE during the adiabatic demagnetization process, which may be of principle importance for the low-temperature magnetic refrigeration. Hence, let us also investigate the adiabatic demagnetization process of the spin-1/2 Ising-Heisenberg double sawtooth ladder under particular adiabatic conditions. In the following, we will study the isentropes (levels of constant entropy) in the $B/J_{\parallel} - T/J_{\parallel}$ plane and the magnetic Grüneisen parameter times temperature, $T\Gamma_B$, as a function of the magnetic field close to the triple and quadruple points, which have been comprehensively described in the previous

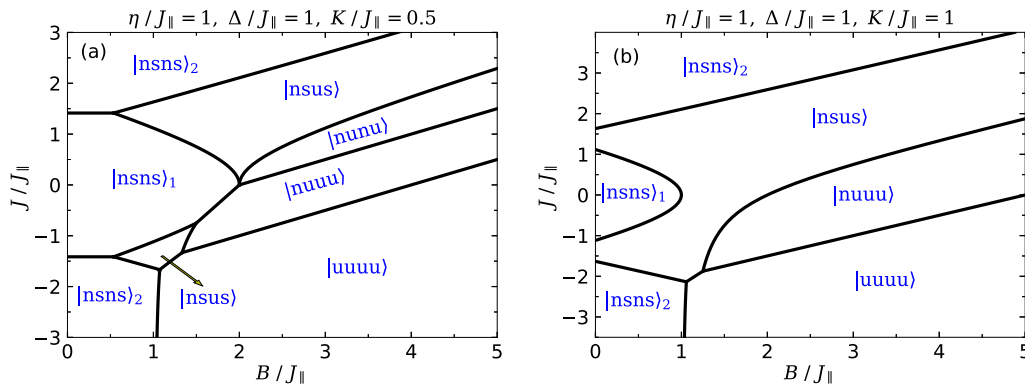


FIG. 7. Ground-state phase diagram of the spin-1/2 double sawtooth ladder in the $J/J_{\parallel} - B/J_{\parallel}$ plane for fixed values of $\eta/J_{\parallel} = J/J_{\parallel} = \Delta/J_{\parallel} = 1$, assuming (a) $K/J_{\parallel} = 0.5$ and (b) $K/J_{\parallel} = 1$. In (a), all multicoexistence points are triple points.

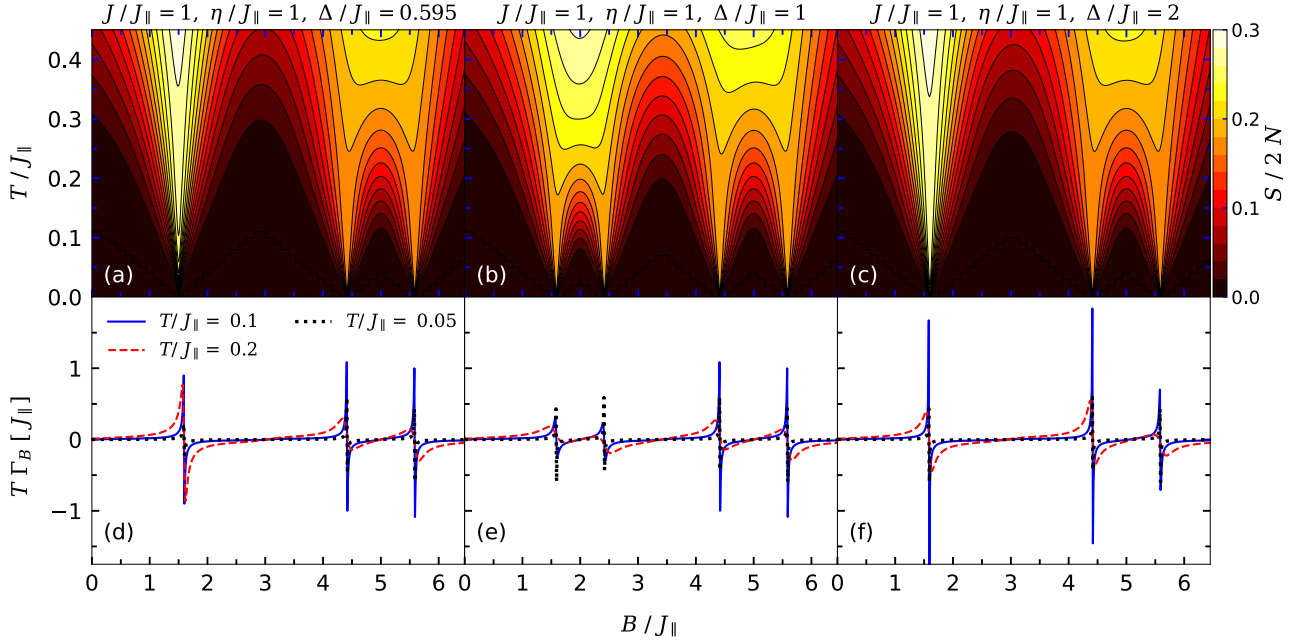


FIG. 8. (a)–(c) Contour plots of the isentropes of the spin-1/2 Ising-Heisenberg double sawtooth ladder in the temperature T/J_{\parallel} versus the magnetic field B/J_{\parallel} plane for the fixed value of $J/J_{\parallel} = \eta/J_{\parallel} = 1$. According to Eq. (10), the four-spin exchange term is taken as $K = K_Q^{\max} \approx 0.2929$ in all panels. In (a), the corresponding coordinates of the first triple point is taken as $\Delta/J_{\parallel} = 0.595$ [see Fig. 5(b)]. In (b), we consider the isotropic coupling constant $\Delta/J_{\parallel} = 1.0$. In (c), according to the coordinates of the quadruple point in Fig. 5(b), we consider the exchange anisotropy as $\Delta/J_{\parallel} = 2.0$. By inspecting Fig. 5(b), each temperature drop occurs near the first-order zero-temperature phase transition. (d)–(f) The magnetic Grüneisen parameter multiplied by temperature $T\Gamma_B$ as a function of magnetic field B/J_{\parallel} for the same set of parameters as (a)–(c), respectively. Three different temperatures $T/J_{\parallel} = (0.05, 0.1, 0.2)$ are considered.

section. The effects of the exchange anisotropy Δ/J_{\parallel} on the entropy and the magnetic cooling rate are investigated as well.

Figures 8(a)–8(c) show the entropy of the spin-1/2 Ising-Heisenberg double sawtooth ladder in the $B/J_{\parallel} - T/J_{\parallel}$ plane by assuming the following parameter values: $J/J_{\parallel} = \eta/J_{\parallel} = 1$ and three different exchange anisotropies $\Delta/J_{\parallel} = (0.595, 1.0, 2.0)$. It is worthwhile to recall that Eq. (10) holds for the particular case $K = K_Q^{\max} \approx 0.2929$ [see horizontal dotted lines in Figs. 6(a)–6(c)]. By comparing Fig. 8(a) with the ground-state phase diagram depicted in Fig. 5(b), one encounters that the sizable MCE in a low-temperature regime with a relatively low value of the entropy $S/4N$ coincides with first-order ground-state phase transitions. It can be understood that if the magnetic field decreases adiabatically from $B/J_{\parallel} = 2.0$ towards the triple point $B/J_{\parallel} = 1.5858$, the temperature dramatically drops down.

By increasing the exchange anisotropy Δ/J_{\parallel} , the value of entropy significantly changes near the critical fields, at which temperature falls down [see Figs. 8(b) and 8(c)]. Evidently, the alterations of entropy $S/4N$ are sharper close to the triple and quadruple points where the temperature drops down more rapidly. Generally, we observe three enhanced regions of MCE accompanied with a relatively fast cooling of the model at two selected coordinates corresponding to the triple and quadruple points of Fig. 5(b) [see Figs. 8(a) and 8(c)]. In Fig. 8(a), the first region of enhanced MCE is due to the existence of the triple point at which three ground states $|\text{nsns}\rangle_1$, $|\text{nsus}\rangle$, and $|\text{nnuu}\rangle$ coexist together. The second region of enhanced MCE is caused by the field-induced ground-state

phase transition from $|\text{nnuu}\rangle$ to $|\text{nnuu}\rangle$, while the third one appears near the field-driven ground-state phase transition from $|\text{nnuu}\rangle$ to $|\text{uuuu}\rangle$. Analogously, it can be observed that the modulation of the interaction parameters Δ/J_{\parallel} and K/J_{\parallel} results in a change of the position of critical points at which the enhanced MCE occurs [see Figs. 8(b) and 8(d)].

Now, let us discuss the effects of the exchange anisotropy and the cyclic four-spin Ising coupling on the magnetic Grüneisen parameter. To this end, we plot in Figs. 8(d)–8(f) the magnetic Grüneisen parameter times temperature, $T\Gamma_B$, against the magnetic field at three different temperatures: $T/J_{\parallel} = (0.05, 0.1, 0.2)$ for the same set of the interaction parameters as used in Figs. 8(a)–8(c), respectively. It follows from Fig. 8(d) that the product $T\Gamma_B$ changes its sign near the triple point emergent at $B/J_{\parallel} \approx 1.5858$, which is closely related to an accumulation of the isentropy lines due to the coexistence of three different ground states. Setting up all parameters such that four ground states $|\text{nsus}\rangle$, $|\text{nnuu}\rangle$, $|\text{usus}\rangle$, and $|\text{nnuu}\rangle$ coexist together at the quadruple point with coordinates $(\Delta/J_{\parallel}, K_Q^{\max}/J_{\parallel}, B_Q^{\max}/J_{\parallel}) = (2.0, 0.2929, 4.4142)$ results in observing a fast cooling/heating of the Ising-Heisenberg system with even larger value of the Grüneisen parameter. Therefore, the magnetic behavior of Grüneisen parameter corroborates that the MCE is considerably enhanced during the adiabatic demagnetization process if the interaction parameters $(K/J_{\parallel}, \Delta/J_{\parallel})$ are tuned close enough to the quadruple point. From the exact results obtained for the entropy and cooling rate of the Ising-Heisenberg double sawtooth ladder shown in Figs. 8(c) and 8(f), one can deduce that the MCE is remarkably

enhanced in a close vicinity of the quadruple point. It could be indeed concluded that the spin-1/2 Ising-Heisenberg double sawtooth ladder exhibits enhanced MCE compared to other ranges of $K/J_{\parallel} \neq K_Q/J_{\parallel}$ whenever Eqs. (10) and (11) hold for each point on the curves plotted in Fig. 4(b).

Another result gained from our examinations is the particular response of the magnetic Grüneisen parameter with respect to temperature variations. We display in Figs. 8(d)–8(f) the product $T\Gamma_B$ as a function of the magnetic field at three different temperatures as well. As usual, increasing the temperature suppresses, in general, the enhanced MCE occurred at critical magnetic fields. The interesting point to declare is that the observed MCE at triple and quadruple points shows an unconventional resistance against the rising temperature. As a matter of fact, the enhanced MCE is sizable close to the triple and quadruple points even at higher temperatures when $\Delta/J_{\parallel} = 2.0$, $K/J_{\parallel} = K_Q/J_{\parallel}$, and the magnetic field is tuned sufficiently close to the critical point B_Q/J_{\parallel} .

III. MAGNETIZATION PROCESS OF THE SPIN-1/2 HEISENBERG DOUBLE SAWTOOTH LADDER

In this section, we proceed to study of the zero-temperature magnetization process of the full quantum spin-1/2 Heisenberg model on the double sawtooth ladder with four-spin Ising coupling in the presence of the external magnetic field. Unlike the previous case, the magnetic ground states of the fully quantum spin-1/2 Heisenberg double sawtooth ladder cannot be rigorously extracted through exact analytical methods and, hence, the ED exploiting the Lanczos algorithm and DMRG methods are used as two numerical techniques to solve the Hamiltonian of the spin-1/2 Heisenberg double sawtooth ladder given by

$$H = \sum_{j=1}^N \left[(\sigma_{1,j} \cdot \sigma_{2,j})_{\eta,\Delta} + \sum_{a=1,2} (J_{\parallel} \sigma_{a,j} \cdot \sigma_{a,j+1} + J \sigma_{a,j} \cdot (\sigma_{a,j-1} + \sigma_{a,j+1})) + J_{\perp} \sigma_{1,j} \cdot \sigma_{2,j} + K \sigma_{1,j}^z \sigma_{1,j+1}^z \sigma_{2,j}^z \sigma_{2,j+1}^z - B \sum_{a=1,2} \sigma_{a,j}^z \right]. \quad (12)$$

By using ED method, we have exactly computed the lowest-energy eigenstates of the spin-1/2 Heisenberg model on the double sawtooth ladder for relatively small finite-size systems up to $N = 12$ rungs (i.e., the total number of spins is 24). These exact numerical results will be subsequently confronted with the DMRG data calculated for the spin-1/2 Heisenberg double sawtooth ladder for larger finite-size systems with $N = 24, 32, 40, 48$ (i.e., the total number of spins are 48, 64, 80, 96, respectively). In our numerical calculations, periodic boundary conditions (PBCs) were implemented such that $N + 1 = 1$. We opt for a total of 25 DMRG sweeps in our analysis. To ensure the precision of the DMRG outcomes in each sweep, we tuned the pertinent parameters, as outlined below:

(1) The maximum bond dimension of the MPS is dynamically adjusted throughout each sweep, reaching a peak value of 2200. This adjustment serves as a pivotal factor in controlling the accuracy of our computations.

(2) The energy cutoff, dictating the threshold for truncation errors in each sweep, is rigorously defined at 10^{-11} . This criterion aids in maintaining the desired level of accuracy.

(3) Introducing a noise term, proportionate to the magnitude of the truncation error, further improves the precision of our results. This step contributes to refining the overall reliability of our computations.

First, let us consider absence of the four-spin coupling (i.e., $K/J_{\parallel} = 0$) to obtain zero-temperature magnetization curves of the full spin-1/2 Heisenberg double sawtooth ladder for two different values of the exchange anisotropy $\Delta/J_{\parallel} = 1$ and $\Delta/J_{\parallel} = 2$ (see Fig. 9). Figure 9 confronts the numerical results for zero-temperature magnetization curves as obtained from the ED and DMRG methods for the fixed values of $\eta/J_{\parallel} = \Delta/J_{\parallel} = J/J_{\parallel} = 1$ and $K/J_{\parallel} = 0$. It is evident from Figs. 9(a)–9(d) that the magnetization curves definitely exhibit zero and one-half magnetization plateaus when the total magnetization is normalized with respect to the saturation magnetization, while the presence of other plateaus is questionable. To shed light on this issue, the width of the intermediate magnetization plateaus at one-quarter, one-half, and three-quarters of the saturation magnetization is plotted in Figs. 10(a)–10(c) for $\Delta/J_{\parallel} = 1$. In Fig. 10(a), one observes that the intermediate one-quarter magnetization plateau gradually shrinks with increasing of the system size and it entirely disappears in the thermodynamic limit $N \rightarrow \infty$. Contrary to this, it is evident from Fig. 10(b) that the width of intermediate one-half magnetization plateau firmly survives in the thermodynamic limit $N \rightarrow \infty$. Last but not least, it follows from Fig. 10(c) that the intermediate three-quarter magnetization plateau gradually disappears in the thermodynamic limit and, hence, it does not represent the true magnetization plateau for $\Delta/J_{\parallel} = 1$. It could be concluded that the intermediate zero- and one-half magnetization plateaus of the spin-1/2 Heisenberg double sawtooth ladder survive in the thermodynamic limit, whereby the analogous intermediate plateaus of the spin-1/2 Ising-Heisenberg double sawtooth ladder correspond to ground states $|\text{nsns}\rangle_1$ and $|\text{nnun}\rangle$. The DMRG simulations of the spin-1/2 Heisenberg double sawtooth ladder thus decisively verify the presence or absence of given intermediate magnetization plateaus in the thermodynamic limit.

The ED and DMRG results for zero-temperature magnetization curves of the spin-1/2 Heisenberg double sawtooth ladder are plotted in Figs. 9(e)–9(h) for the particular case $\Delta/J_{\parallel} = 2$. It could be anticipated that the magnetization curves of the spin-1/2 Heisenberg double sawtooth ladder may display intermediate magnetization plateaus at zero, one-quarter, and one-half of the saturation magnetization even for a very large number of spins. Based on the DMRG calculations, it can be conjectured that two intermediate magnetization plateaus at one-quarter and one-half of the saturation magnetization are indeed the actual magnetization plateaus persisting in the thermodynamic limit. To bear evidence of this statement we plot in Figs. 10(d)–10(f) the width of the intermediate magnetization plateaus against the inverse value of the total number of spins, including results extrapolated to the thermodynamic limit. For the two aforementioned intermediate magnetization plateaus, the lower and upper edges of the intermediate magnetization plateaus do not

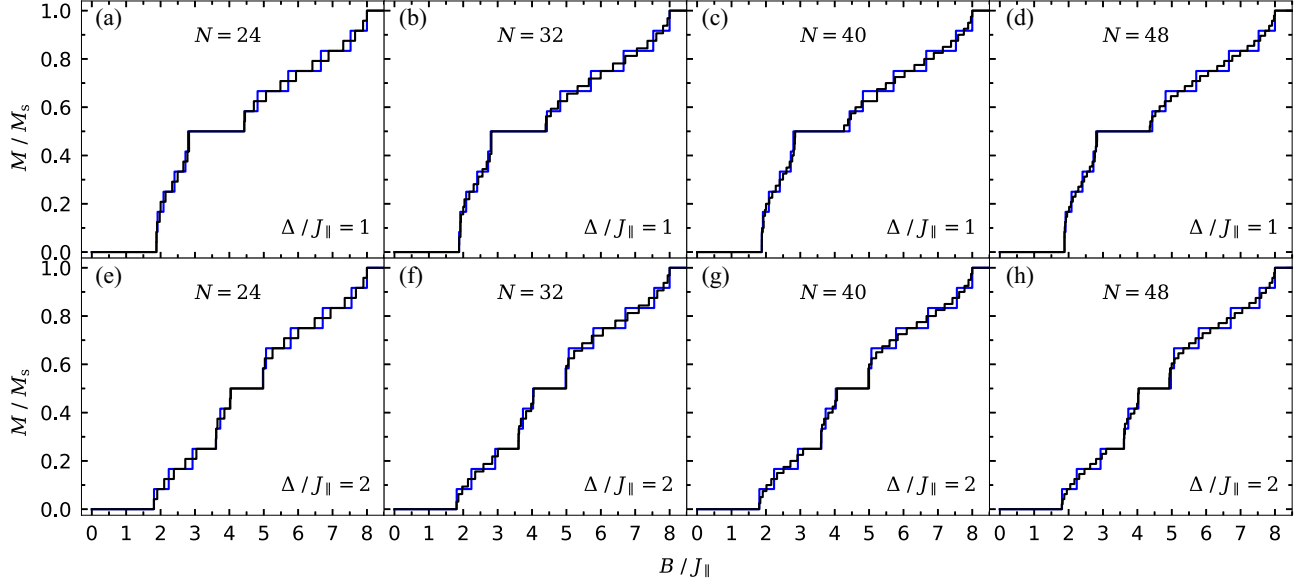


FIG. 9. Full ED (blue lines) and DMRG (black lines) results for zero-temperature magnetization curves of the spin-1/2 Heisenberg double sawtooth ladder. The interaction ratios $\eta/J_{\parallel} = J/J_{\parallel} = 1$ and $K/J_{\parallel} = 0$ are considered in all panels. The ED data were obtained for $N = 12$, whereas the DMRG data were obtained for the following set of parameters: (a) $\Delta/J_{\parallel} = 1$, $N = 24$; (b) $\Delta/J_{\parallel} = 1$, $N = 32$; (c) $\Delta/J_{\parallel} = 1$, $N = 40$; (d) $\Delta/J_{\parallel} = 1$, $N = 48$; (e) $\Delta/J_{\parallel} = 2$, $N = 24$; (f) $\Delta/J_{\parallel} = 2$, $N = 32$; (g) $\Delta/J_{\parallel} = 2$, $N = 40$; (h) $\Delta/J_{\parallel} = 2$, $N = 48$.

converge in the thermodynamic limit to the same asymptotic value, which means that they both represent true intermediate magnetization plateaus of the full spin-1/2 Heisenberg double sawtooth ladder with $\Delta/J_{\parallel} = 2$. Similarly as in the previous case, the intermediate plateau at three-quarters of the saturation magnetization may not be a true plateau because

the associated energy gap is closed when extrapolated to the thermodynamic limit.

It can be concluded that the intermediate magnetization plateaus at zero and one-half of the saturation magnetization for $\Delta/J_{\parallel} = 1$ [see Figs. 9(a)–9(d)], and at zero, one-quarter, and one-half of the saturation magnetization for

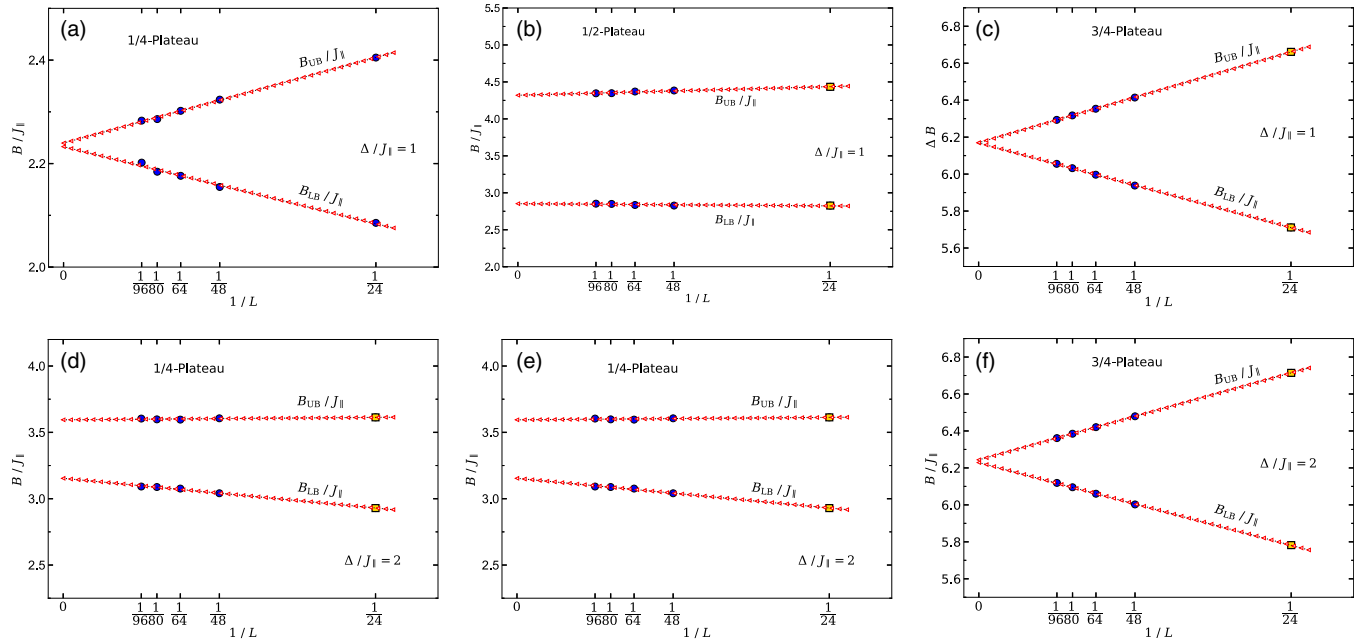


FIG. 10. The magnetic fields B_{LB}/J_{\parallel} and B_{UB}/J_{\parallel} corresponding to lower and upper bounds of the intermediate magnetization plateaus (DMRG data: circles, ED data: squares) together with the relevant extrapolation to the thermodynamic limit $N \rightarrow \infty$ by considering (a) one-quarter plateau for $\Delta/J_{\parallel} = 1$, (b) one-half plateau for $\Delta/J_{\parallel} = 1$, (c) three-quarter plateau for $\Delta/J_{\parallel} = 1$, (d) one-quarter plateau for $\Delta/J_{\parallel} = 2$, (e) one-half plateau for $\Delta/J_{\parallel} = 2$, (f) three-quarter plateau for $\Delta/J_{\parallel} = 2$.

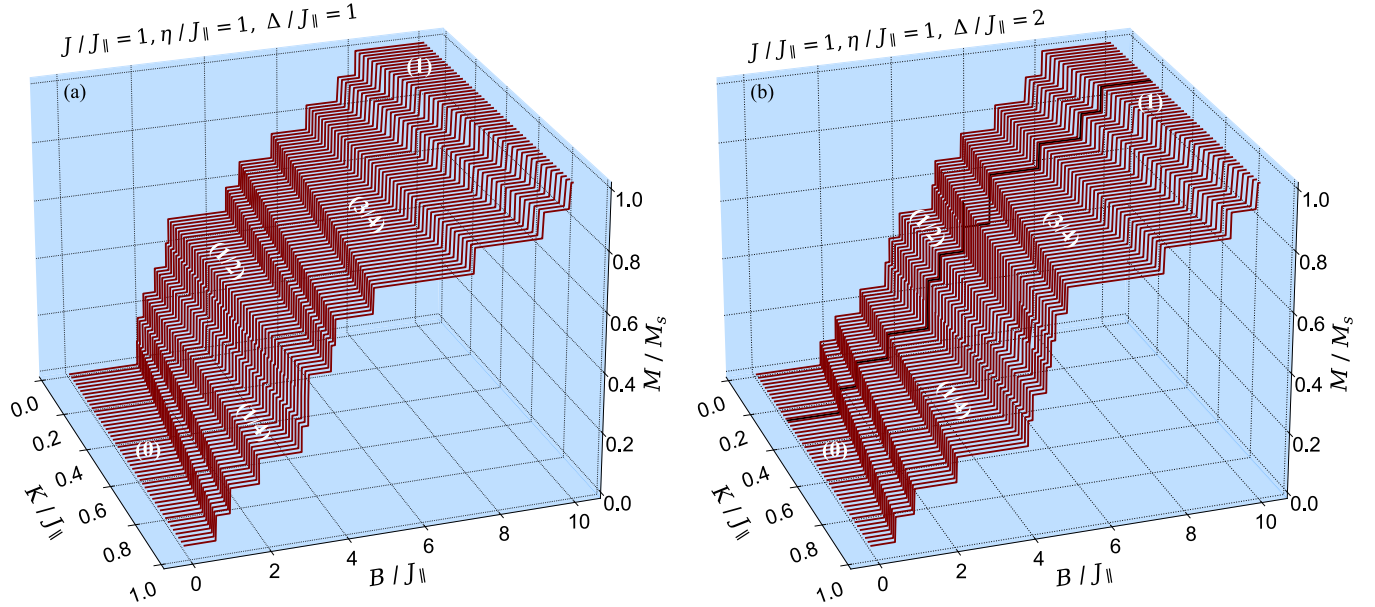


FIG. 11. 3D plot of the zero-temperature magnetization of the spin-1/2 quantum Heisenberg double sawtooth ladder as a function of the magnetic field B/J_{\parallel} and four-spin exchange interaction K/J_{\parallel} for fixed value of the interaction parameters $\eta/J_{\parallel} = J/J_{\parallel} = 1$ and two selected values of the exchange anisotropy: (a) $\Delta/J_{\parallel} = 1$, (b) $\Delta/J_{\parallel} = 2$. Here, we consider finite-size system characterized by $N = 12$, and we employ the ED method.

$\Delta/J_{\parallel} = 2$ [see Figs. 9(e)–9(h)] represent the actual magnetization plateaus. To complete our discussion, we study the effect of four-spin Ising coupling on the magnetization process of the spin-1/2 Heisenberg model on the double sawtooth ladder. Three-dimensional zero-temperature plot of the magnetization of the spin-1/2 Heisenberg double sawtooth ladder is presented in Fig. 11 as a function of the magnetic field B/J_{\parallel} and the cyclic four-spin Ising interaction K/J_{\parallel} .

Figure 11(a) displays the magnetization normalized with respect to its saturation value as a function of the magnetic field and four-spin Ising interaction for fixed values of the interaction parameters $\eta/J_{\parallel} = J/J_{\parallel} = 1$ and $\Delta/J_{\parallel} = 1$. We investigate a finite-size system consisting of 24 spins ($N = 12$) through the utilization of the ED method. It is worthwhile to recall that the magnetization curve displays for $K/J_{\parallel} = 0$ two actual intermediate magnetization plateaus at zero and one-half of the saturation magnetization (based on our DMRG results shown in Fig. 9). With increase of the four-spin coupling K/J_{\parallel} , one observes substantial changes of the magnetization curve with a gradual shrinking of zero and one-half magnetization plateaus, whereas the intermediate one-quarter plateau contrarily becomes broader. It is quite plausible to conjecture that there are accordingly strong indications for the appearance of the one-quarter and three-quarter magnetization plateaus for nonzero values of the Ising four-spin interaction K/J_{\parallel} . Opposite to this, the intermediate one-half magnetization plateau may terminate for nonzero K/J_{\parallel} at a special quantum critical point. If we turn back to Fig. 6(b), we find that a similar scenario happens also for the one-half magnetization plateau of the spin-1/2 Ising-Heisenberg double sawtooth ladder corresponding to ground state $|\text{nunu}\rangle$, which gradually shrinks upon increasing the four-spin coupling K/J_{\parallel} and ultimately terminates at a critical point with the coordinates $(K/J_{\parallel}, B/J_{\parallel}) \approx (0.8, 3.4142)$.

Even more striking features can be figured out in the magnetization curves plotted in Fig. 11(b) for $\Delta/J_{\parallel} = 2$. Based on the DMRG results shown in Fig. 9, it is obvious that the magnetization curve of the spin-1/2 Heisenberg double sawtooth ladder exhibits for $\Delta/J_{\parallel} = 2$ and $K/J_{\parallel} = 0$ three intermediate plateaus at zero, one-quarter, and one-half of the saturation magnetization together with three gapless spin-liquid regions separating them. The full ED calculations unveil that the intermediate one-half magnetization plateau becomes narrower upon increasing the four-spin Ising interaction K/J_{\parallel} . By inspecting Fig. 6(b), one can realize that in the ground-state phase diagram of the spin-1/2 Ising-Heisenberg double sawtooth ladder the area of the ground state $|\text{nunu}\rangle$ ($|\text{usus}\rangle$) corresponds to the one-half magnetization plateau and also gradually decreases upon increasing the four-spin coupling K/J_{\parallel} until it disappears at a quadruple point $(K_Q/J_{\parallel}, B_Q/J_{\parallel}) \approx (0.2929, 4.4142)$. On the other hand, the parameter region corresponding to the other ground state $|\text{nuuu}\rangle$ related to the three-quarter magnetization plateau increases upon increasing the four-spin interaction term K/J_{\parallel} .

IV. CONCLUSIONS

In this paper, we have exactly solved the spin-1/2 Ising-Heisenberg double sawtooth ladder supplemented with the four-spin Ising interaction by taking advantage of the classical transfer-matrix technique. The ground-state phase diagram, the magnetocaloric properties, and magnetic Grüneisen parameter of this model were rigorously examined. We found a peculiar quadruple point in the ground-state phase diagram at which four different ground states coexist together, whereby this quadruple point cannot be observed for the pure Ising double sawtooth ladder. Besides, the enhanced MCE has been detected near the triple and quadruple points. The exact results

for the isentropes of the spin-1/2 Ising-Heisenberg double sawtooth ladder evidenced a fast cooling during the adiabatic demagnetization process when the magnetic field is tuned to a close vicinity of the triple and quadruple points. The coordinates of the quadruple point depends on a relative ratio between the isotropic exchange interaction between the Heisenberg dimers and the nearest-neighbor Ising interaction along the legs. For a particular value of the four-spin Ising interaction that drives the investigated spin-1/2 Ising-Heisenberg model to a quadruple point, one even detects the enhanced MCE at relatively high temperatures.

By employing the numerical ED and DMRG methods, we also investigated the magnetization process of the spin-1/2 Heisenberg double sawtooth ladder with and without the four-spin Ising coupling. A proper finite-size analysis allowed us to discern the true intermediate magnetization plateaus from the gapless quantum spin-liquid regions. The ED data imply that the intermediate one-half magnetization plateau gradually shrinks upon increasing the four-spin Ising coupling and seems to vanish at a special quantum critical point. A gradual suppression of the gapped one-half plateau phase due to the rising four-spin Ising interaction, which possibly closes an energy gap, might be an indication of the Kosterlitz-Thouless quantum critical point. The precise nature of the quantum critical point can be an interesting subject of future studies.

ACKNOWLEDGMENTS

H.A.Z. acknowledges the financial support of the National Scholarship Programme of the Slovak Republic (NŠP). V.O. acknowledges partial financial support from ANSEF (Grants No. PScondmatth-2462 and No. PS-condmatrth-2884), A.Z. and J.S. acknowledge financial support by the grant of the Slovak Research and Development Agency provided under Contract No. APVV-22-0172 and by a grant of The Ministry of Education, Science, Research, and Sport of the Slovak Republic provided under Contract No. VEGA 1/0695/23. A.Z. acknowledges the financial support provided by the Development Agency under Grant No. VVGS-2023-2559.

APPENDIX A

The following term presents a comprehensive description of the cyclic four-spin exchange:

$$H_{\text{ring}} = \sum_{j=1}^N K[(s_{1,j} \cdot s_{1,j+1})(s_{2,j+1} \cdot s_{2,j}) + (s_{1,j} \cdot s_{2,j})(s_{1,j+1} \cdot s_{2,j+1}) - (s_{1,j} \cdot s_{2,j+1})(s_{1,j+1} \cdot s_{2,j})], \quad (\text{A1})$$

where $s_a \cdot s_b = s_a^x s_b^x + s_a^y s_b^y + s_a^z s_b^z$. In the present paper, we consider solely the z components of the spin operators to contribute to the anisotropic segment of the Hamiltonian. As a result, the expression for the cyclic four-spin term takes on a straightforward form:

$$H_{\text{ring}}^z = \sum_{j=1}^N K s_{1,j}^z s_{1,j+1}^z s_{2,j+1}^z s_{2,j}^z. \quad (\text{A2})$$

APPENDIX B

The eigenvalues of the quantum part of the Hamiltonian Eq. (7) are

$$\varepsilon_{1,2} = -\Delta \pm \sqrt{J^2(s_{1,j} - s_{2,j} + s_{1,j+1} - s_{2,j+1})^2 + \eta^2},$$

$$\varepsilon_{3,4} = \Delta \pm [2B - J(s_{1,j} + s_{2,j} + s_{1,j+1} + s_{2,j+1})], \quad (\text{B1})$$

and the corresponding eigenvectors are given by

$$|\varphi_{1,2}\rangle = \frac{1}{\sqrt{1 + A_{\pm}^2}}(|\uparrow\downarrow\rangle + A_{\pm}|\downarrow\uparrow\rangle), \quad (\text{B2})$$

$$|\varphi_3\rangle = |\downarrow\downarrow\rangle,$$

$$|\varphi_4\rangle = |\uparrow\uparrow\rangle,$$

where

$$A_{\pm} = \frac{1}{\eta} [J(s_{2,j} - s_{1,j} + s_{2,j+1} - s_{1,j+1}) \pm \sqrt{J^2(s_{2,j} - s_{1,j} + s_{2,j+1} - s_{1,j+1})^2 + \eta^2}]. \quad (\text{B3})$$

The explicit form of the 4×4 transfer matrix is

$$\mathbf{T} = \begin{pmatrix} z_1^{-1} z_2^{-1} \lambda^{-1} \mu^2 (\chi_0 + \psi_2) & z_2^{-1} \lambda \mu^2 (\chi_1 + \psi_1) & z_2^{-1} \lambda \mu^2 (\chi_1 + \psi_1) & z_1 z_2^{-1} \lambda^{-1} \mu^2 (\chi_0 + \psi_0) \\ z_2 \lambda (\chi_1 + \psi_1) & z_1 z_2^{-1} \lambda (\chi_2 + \psi_0) & z_1 z_2 \lambda^{-1} (\chi_0 + \psi_0) & z_2 \lambda (\chi_1 + \psi_{-1}) \\ z_2 \lambda (\chi_1 + \psi_1) & z_1 z_2 \lambda^{-1} (\chi_0 + \psi_0) & z_1^{-1} z_2 \lambda^{-1} (\chi_2 + \psi_0) & z_2 \lambda (\chi_1 + \psi_{-1}) \\ z_1 z_2^{-1} \lambda^{-1} \mu^{-2} (\chi_0 + \psi_0) & z_2^{-1} \lambda^{-1} \mu^{-2} (\chi_1 + \psi_{-1}) & z_2^{-1} \lambda^{-1} \mu^{-2} (\chi_1 + \psi_{-1}) & z_1^{-1} z_2^{-1} \lambda^{-1} \mu^{-2} (\chi_0 + \psi_{-2}) \end{pmatrix}, \quad (\text{B4})$$

where the following notations are adopted:

$$z_1 = e^{2\beta J_{\parallel}}, \quad z_2 = e^{\beta J_{\perp}}, \quad \lambda = e^{\beta K}, \quad \mu = e^{\beta B},$$

$$\chi_n = 2e^{\beta \Delta} \cosh \frac{\beta}{2} \sqrt{(2nJ)^2 + \eta^2}, \quad n = 0, 1, 2,$$

$$\psi_n = 2e^{-\beta \Delta} \cosh(\beta(B - nJ)), \quad n = -2, -1, 0, 1, 2. \quad (\text{B5})$$

- [1] A. S. Oja and O. V. Lounasmaa, *Rev. Mod. Phys.* **69**, 1 (1997).
- [2] K. A. Gschneider Jr., V. K. Pecharsky, and A. O. Tsokol, *Rep. Prog. Phys.* **68**, 1479 (2005).
- [3] M. E. Zhitomirsky and A. Honecker, *J. Stat. Mech.: Theory Exp.* (2004) P07012.
- [4] A. Honecker and M. E. Zhitomirsky, *J. Phys.: Conf. Ser.* **145**, 012082 (2009).
- [5] A. Honecker and S. Wessel, *Condens. Matter Phys.* **12**, 399 (2009).
- [6] C. Trippé, A. Honecker, A. Klümper, and V. Ohanyan, *Phys. Rev. B* **81**, 054402 (2010).
- [7] M. Topilko, T. Krokhumalskii, O. Derzhko, and V. Ohanyan, *Eur. Phys. J. B* **85**, 278 (2012).
- [8] L. Gálisová, *Condens. Matter Phys.* **17**, 13001 (2014).
- [9] J. Strečka, K. Karlová, and T. Madaras, *Physica B* **466-467**, 76 (2015).
- [10] K. Karlová, J. Strečka, and J. Richter, *J. Phys.: Condens. Matter* **29**, 125802 (2017).
- [11] K. Karlova and J. Strečka, *J. Low Temp. Phys.* **187**, 727 (2017).
- [12] M. Žukovič and M. Semjan, *J. Magn. Magn. Mater.* **451**, 311 (2018).
- [13] C. Beckmann, J. Ehrens, and J. Schnack, *J. Magn. Magn. Mater.* **482**, 113 (2019).
- [14] V. Ohanyan and A. Honecker, *Phys. Rev. B* **86**, 054412 (2012).
- [15] J. Strečka, O. Rojas, T. Verkholyak, and M. L. Lyra, *Phys. Rev. E* **89**, 022143 (2014).
- [16] L. Gálisová, *J. Phys.: Condens. Matter* **28**, 476005 (2016).
- [17] J. Torrico, M. Rojas, S. M. de Souza, and O. Rojas, *Phys. Lett. A* **380**, 3655 (2016).
- [18] R. C. Alécio, J. Strečka, and M. L. Lyra, *J. Magn. Magn. Mater.* **451**, 218 (2018).
- [19] L. Gálisová and D. Knežo, *Phys. Lett. A* **382**, 2839 (2018).
- [20] J. Strečka, M. Jaščur, M. Hagiwara, Y. Narumi, K. Kindo, and K. Minami, *Phys. Rev. B* **72**, 024459 (2005).
- [21] W. Van den Heuvel and L. F. Chibotaru, *Phys. Rev. B* **82**, 174436 (2010).
- [22] S. Bellucci, V. Ohanyan, and O. Rojas, *Europhys. Lett.* **105**, 47012 (2014).
- [23] S. Sahoo, J. P. Sutter, and S. Ramasesha, *J. Stat. Phys.* **147**, 181 (2012).
- [24] J. Strečka, M. Hagiwara, Y. Han, T. Kida, Z. Honda, and M. Ikeda, *Condens. Matter Phys.* **15**, 43002 (2012).
- [25] Y. Han, T. Kida, M. Ikeda, M. Hagiwara, J. Strečka, and Z. Honda, *J. Korean Phys. Soc.* **62**, 2050 (2013).
- [26] F. Souza, L. M. Veríssimo, J. Strečka, M. L. Lyra, and M. S. S. Pereira, *Phys. Rev. B* **102**, 064414 (2020).
- [27] J. Strečka, L. Gálisová, and T. Verkholyak, *Condens. Matter Phys.* **23**, 43708 (2020).
- [28] L. Gálisová, *J. Magn. Magn. Mater.* **561**, 169721 (2022).
- [29] M. Roger, J. H. Hetherington, and J. M. Delrieu, *Rev. Mod. Phys.* **55**, 1 (1983).
- [30] M. Müller, T. Vekua, and H. J. Mikeska, *Phys. Rev. B* **66**, 134423 (2002).
- [31] T. A. Arakelyan, V. R. Ohanyan, L. N. Ananikyan, N. S. Ananikian, and M. Roger, *Phys. Rev. B* **67**, 024424 (2003).
- [32] V. Ohanyan, and N. Ananikian, in *Mathematical Physics Proceedings of the XI Regional Conference, Tehran, Iran, 2004*, edited by S. Rahvar, N. Sadooghi, and F. Shojai (World Scientific, Singapore, 2005), pp. 49–51.
- [33] L. N. Ananikyan, *Int. J. Mod. Phys. B* **21**, 755 (2007).
- [34] V. V. Hovhannisyanyan, R. G. Ghulghazaryan, and N. S. Ananikian, *Physica A* **388**, 1479 (2009).
- [35] N. S. Ananikian, L. N. Ananikian, and H. A. Lazaryan, *Phys. Atom. Nucl.* **75**, 1250 (2012).
- [36] L. Gálisová, *Phys. Status Solidi B* **250**, 187 (2013).
- [37] H. Arian Zad and N. Ananikian, *J. Phys.: Condens. Matter* **29**, 455402 (2017).
- [38] H. Arian Zad and N. Ananikian, *J. Phys.: Condens. Matter* **30**, 165403 (2018).
- [39] H. Arian Zad and N. Ananikian, *Solid State Commun.* **276**, 24 (2018).
- [40] V. Ohanyan, *Condens. Matter Phys.* **12**, 343 (2009).
- [41] S. Bellucci and V. Ohanyan, *Eur. Phys. J. B* **75**, 531 (2010).
- [42] S. Bellucci and V. Ohanyan, *Eur. Phys. J. B* **86**, 446 (2013).
- [43] T. Verkholyak and J. Strečka, *Condens. Matter Phys.* **16**, 13601 (2013).
- [44] J. Strečka, L. Gálisová, and T. Verkholyak, *Phys. Rev. E* **101**, 012103 (2020).
- [45] F. Amiri, G. Sun, H.-J. Mikeska, and T. Vekua, *Phys. Rev. B* **92**, 184421 (2015).
- [46] T. Sugimoto, M. Mori, T. Tohyama, and S. Maekawa, *Phys. Rev. B* **87**, 155143 (2013).
- [47] B. Koteswararao, S. Salunke, A. V. Mahajan, I. Dasgupta, and J. Bobroff, *Phys. Rev. B* **76**, 052402 (2007).
- [48] O. Mentré, E. Janod, P. Rabu, M. Hennion, F. Leclercq-Hugeux, J. Kang, C. Lee, M.-H. Whangbo, and S. Petit, *Phys. Rev. B* **80**, 180413(R) (2009).
- [49] B. Koteswararao, A. V. Mahajan, L. K. Alexander, and J. Bobroff, *J. Phys.: Condens. Matter* **22**, 035601 (2010).
- [50] P. Weinberg and M. Bukov, *SciPost Phys.* **2**, 003 (2017).
- [51] P. Weinberg and M. Bukov, *SciPost Phys.* **7**, 020 (2019).
- [52] M. Fishman, S. R. White, and E. M. Stoudenmire, *SciPost Phys. Codebases* **4** (2022).

Correction: Support information in the Acknowledgment section was incomplete and has been fixed.